REVIEW SUMMARY

MATERIALS SCIENCE

Atomic electron tomography: 3D structures without crystals

Jianwei Miao,* Peter Ercius, Simon J. L. Billinge

BACKGROUND: To understand material properties and functionality at the most fundamental level, one must know the three-dimensional (3D) positions of atoms with high precision. For crystalline materials, x-ray crystallography has provided this information since the pioneering work of Max von Laue, William Henry Bragg, and William Lawrence Bragg around 100 years ago. But perfect crystals are rare in nature. Real materials often contain defects, surface reconstructions, nanoscale heterogeneities, and disorders, which strongly influence material properties and performance. Completely different approaches from crystallography are needed to determine the 3D atomic arrangement of crystal defects and noncrystalline systems. Although single-particle cryo–electron microscopy (cryo-EM) has been under rapid development for 3D structure determination of macromolecules with identical or similar conformations at near-atomic resolution, this method cannot be generally applied to the physical sciences for the following three reasons. First, most materials do not have identical copies and cannot be averaged to achieve atomic resolution. Second, a priori knowledge of the peptide sequence and stereochemistry in protein molecules greatly facilitates their 3D atomic structure determination, but this knowledge is not applicable to physical science samples. Third, unlike in biological specimens, the presence of diffraction and phase contrast in the transmission electron microscopy images of most materials poses a challenge for tomographic reconstruction. These difficulties have made the objective of solving the 3D atomic structure of crystal defects and noncrystalline systems a major challenge for structural characterization in the physical sciences.

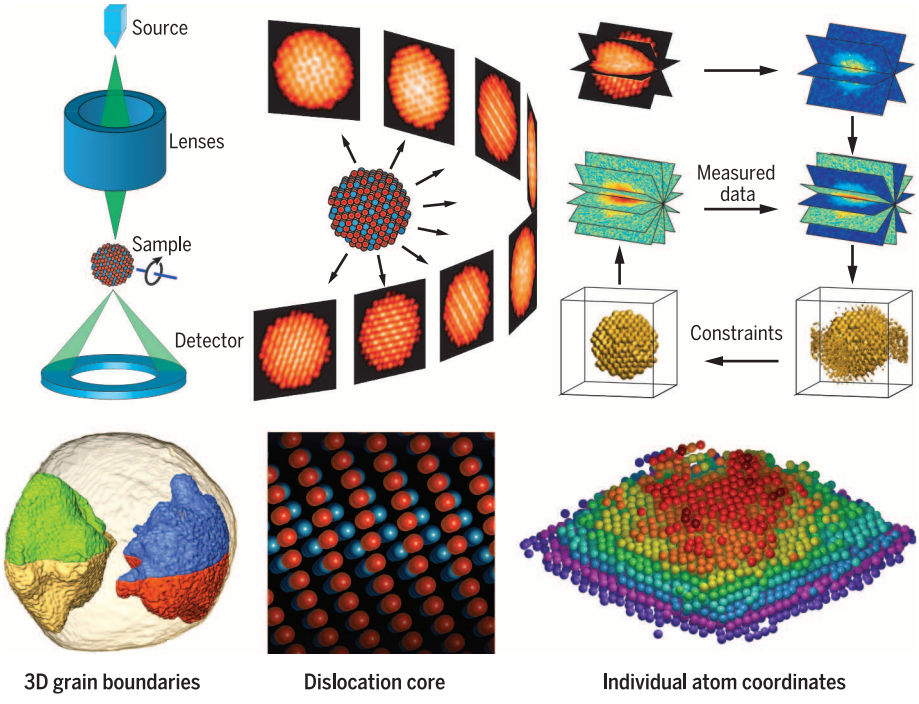

Atomic electron tomography (AET) and its transformative impact on the physical sciences. (**Top**) Schematic diagram of AET, in which 2D images are measured with an advanced electron microscope by tilting a sample to many different orientations. The 3D structure of the sample is iteratively reconstructed from the images, and the coordinates of individual atoms are localized. (**Bottom**) AET enables 3D imaging of crystal defects—such as grain boundaries, stacking faults, dislocations, and point defects—at atomic resolution. The ability to precisely determine the 3D coordinates of individual atoms allows direct measurements of atomic displacements and the full strain tensor in materials.

ADVANCES: Major developments in aberration-corrected electron microscopes, advanced detectors, data acquisition methods, powerful 3D image reconstruction, and atom-tracing algorithms have placed one method—atomic electron tomography (AET)—on the cusp of this breakthrough. In recent years, AET has been used to image the 3D structure of grain boundaries and stacking faults and the 3D core structure of edge and screw dislocations at atomic resolution. This technique has also revealed the existence of atomic steps at 3D twin boundaries that are hidden in conventional 2D projections. Furthermore, the combination of AET and atom-tracing algorithms has enabled the determination of the coordinates of individual atoms and point defects in materials with a 3D precision of ~19 pm, allowing direct measurements of 3D atomic displacements and the full strain tensor. Finally, the single-particle reconstruction method developed in cryo-EM has been applied for 3D structure determination of small (≤2-nm) gold nanoparticles and heterogeneous platinum nanocrystals at atomic-scale resolution.

ON OUR WEBSITE

Read the full article at http://dx.doi.org/10.1126/science.aaf2157

OUTLOOK: The future research frontiers of AET involve increasing the sample complexity (including real materials with different atomic species and disordered systems), image contrast (determining the 3D atomic positions of both heavy and light elements), detection sensitivity (revealing individual atoms at surfaces and interfaces), and data acquisition speed (probing the dynamics of individual atoms and defects). The ability to precisely determine all atomic coordinates and species in real materials without assuming crystallinity will transform our understanding of structure-property relationships at the most fundamental level. For instance, using atomic coordinates as inputs to first-principles calculations, it is possible to compute the effect on the material properties of each defect and atomic reorganization, giving precious clues about how to modify and engineer materials at the atomic level to yield better performance in a device. Catalysis involves atoms interacting on nanoparticle surfaces in poorly understood ways, and the mechanisms of particle growth in synthesis reactors or in devices under load are largely unknown. Breakthroughs in our ability to reliably measure this information in 3D will have effects across disciplines from electronics and catalysis to energy conversion. ■

The list of author affiliations is available in the full article online.
*Corresponding author. Email: miao@physics.ucla.edu
Cite this article as J. Miao *et al.*, *Science* **353**, aaf2157 (2016).
DOI: 10.1126/science.aaf2157

REVIEW

MATERIALS SCIENCE

Atomic electron tomography: 3D structures without crystals

Jianwei Miao,[1]* Peter Ercius,[2] Simon J. L. Billinge[3,4]

Crystallography has been fundamental to the development of many fields of science over the last century. However, much of our modern science and technology relies on materials with defects and disorders, and their three-dimensional (3D) atomic structures are not accessible to crystallography. One method capable of addressing this major challenge is atomic electron tomography. By combining advanced electron microscopes and detectors with powerful data analysis and tomographic reconstruction algorithms, it is now possible to determine the 3D atomic structure of crystal defects such as grain boundaries, stacking faults, dislocations, and point defects, as well as to precisely localize the 3D coordinates of individual atoms in materials without assuming crystallinity. Here we review the recent advances and the interdisciplinary science enabled by this methodology. We also outline further research needed for atomic electron tomography to address long-standing unresolved problems in the physical sciences.

Perfect crystals are rare in nature, and much of our modern science and technology depends on crystals with defects and noncrystalline systems (*1*–*7*). In fact, these systems are the rule rather than the exception; they include high-strength structural materials (dislocations and grain boundaries) (*1*, *2*), information processing (defects and dopants in semiconductors) (*3*), heterogeneous catalysis (reactions on nanoparticle surfaces) (*7*), renewable energy (amorphous silicon) (*8*), energy storage (solid electrolyte glasses and oxides) (*9*), telecommunication and computer networking (optical fibers) (*10*), high-efficiency transformers (metallic glasses) (*6*), and nonvolatile memory (amorphous-crystalline transitions) (*11*). In these applications, it is not just the average structure but also the defects and crystalline imperfections that need to be engineered to obtain the desired properties. Presently, several methods can be used to image crystal defects and noncrystalline specimens, but each has its limitations. Transmission electron microscopy (TEM) has long been used to produce images of crystal defects and dislocations at atomic resolution (*12*), but these are two-dimensional (2D) projection images and are not fully representative of the underlying 3D structures (*13*, *14*). Scanning probe microscopy can provide subatomic resolution only for surface structure (*15*). Although coherent diffractive imaging can determine the 3D structure of noncrystalline specimens and nanocrystals at the nanoscale resolution (*16*–*18*), it requires the further development of coherent x-ray and electron sources, detectors, and advanced image reconstruction algorithms to achieve 3D atomic resolution (*19*–*22*). Atom probe tomography enables the 3D reconstruction of billions of atoms from a tip specimen but cannot offer true atomic resolution because of imperfect spatial resolution and limited detection efficiency (*23*, *24*).

One powerful method to address this major challenge that is under rapid development in both the physical and biological sciences is electron tomography. Electron tomography was developed in 1968 (*25*–*27*) and has been primarily applied to image the 3D structure of biological specimens by rapidly freezing them at cryogenic temperatures (*28*). For cells and cellular organelles, cryo–electron tomography can achieve a 3D resolution of 2 to 5 nm (*29*–*31*), which is mainly limited by radiation damage to the sample (*32*). For large protein molecules with identical or similar conformations, single-particle cryo–electron microscopy (cryo-EM) has been used to image the average 3D structure at near-atomic resolution without the need for crystallization (*33*–*37*), driven by the recent advances in direct electron detectors (*38*), image processing, and reconstruction methods (*39*, *40*). However, these methods cannot be generally applied to solve the 3D atomic structure of physical science samples for the following three reasons. First, most materials do not have identical copies and therefore cannot be averaged to achieve atomic resolution. For example, from one crystallite to another, the structure of a dislocation will be similar (there is a well-defined structural solution) (*1*, *2*), but the location of the dislocation at the atomic scale will differ. Averaging over different crystallites will eliminate the signal of the defect. Thus, we need a method sensitive enough to detect the 3D positions of individual atoms buried in a single object. Second, for protein molecules, a priori knowledge such as the atomic structure of amino acid residues and the peptide sequence of the molecules provides important constraints that greatly reduce the experimental information required for their 3D structure determination (*41*). This knowledge is not applicable to physical science samples. Third, unlike biological specimens, diffraction and phase contrast in the TEM images of most physical science samples prevent the direct application of tomographic reconstruction (*13*, *14*) and require greater ingenuity to solve the reconstruction problem. Despite these challenges, the past few years have seen breakthroughs in the development of atomic electron tomography (AET), which enables 3D structure determination of crystal defects and potentially disordered systems at atomic resolution (*42*–*51*). Here we review the recent advances of AET and the interdisciplinary science enabled by this methodology.

Aberration-corrected electron microscopy

The first TEM to surpass the resolution of the optical microscope was built by Ernst Ruska in the 1930s (*52*). During early research to further improve this instrument, Otto Scherzer realized that a TEM's resolution would always substantially underperform relative to the expected wavelength of the accelerated electrons because of geometrical aberrations inherent to the round electron lenses themselves (known as the Scherzer theorem) (*53*). The most limiting of these aberrations is the well-known third-order spherical aberration, which cannot be corrected with a round lens. In 1947, the use of optical elements with nonrotational symmetry was proposed to compensate for this inherent limitation (*54*). In effect, a set of lenses could be devised that created the exact opposite effect of the aberrations induced by a conventional round lens, and the two effects would cancel out.

Decades of research and development in this area have led to the current generation of aberration-corrected electron microscopes (*55*–*58*), which reach ~0.5 Å resolution with much-improved contrast (*59*). Such high-resolution and high-contrast images benefit the AET reconstruction, allowing precise determination of the 3D coordinates of individual atoms in materials (*49*). Increases in signal-to-noise ratio and image quality also reduce the required beam dose delivered to the sample. On the other hand, aberration-corrected electron lenses reduce the depth of field and limit the sample thickness (*60*). This problem can be overcome by acquiring a through-focal series at each tilt angle. Furthermore, the limited depth of field can also be used as an advantage for observing depth-dependent atomic structures in crystals (*61*). Collectively, the combination of aberration-corrected electron microscopes and AET will greatly facilitate the

[1]Department of Physics and Astronomy and California NanoSystems Institute, University of California, Los Angeles, CA 90095, USA. [2]National Center for Electron Microscopy, Molecular Foundry, Lawrence Berkeley National Laboratory, Berkeley, CA 94720, USA. [3]Department of Applied Physics and Applied Mathematics, Columbia University, 200 Mudd Building, 500 West 120th Street, New York, NY 10027, USA. [4]Department of Condensed Matter Physics and Materials Science, Brookhaven National Laboratory, Upton, NY 11973, USA.
*Corresponding author. Email: miao@physics.ucla.edu

3D characterization of materials at the single-atom level.

Atomic STEM tomography

Acquisition of tomographic tilt series

Although TEM-based tomography has been widely applied in the biological sciences (*29*–*31*, *33*–*37*), a major limitation for the physical science application is the presence of diffraction and phase contrast (*13*, *14*, *62*, *63*). This limitation can be overcome by using the scanning transmission electron microscopy (STEM) mode and an annular dark-field (ADF) detector (*64*–*70*). In ADF-STEM, an electron beam is focused to a small spot and scanned over a sample to form a 2D image (Fig. 1A). The scattered signal at each scanning position is recorded by the ADF detector, which consists of a sensitive annular region with inner and outer angles ranging from a few tens to several hundreds of milliradians, respectively (*71*–*73*). By measuring the signal only at high angles, ADF-STEM satisfies the incoherent imaging approximation in which diffraction and phase contrast are substantially suppressed and the image intensity is approximately proportional to the sample thickness and the atomic number as $Z^{1.8}$ (*71*–*73*). To acquire a tomographic tilt series, the sample is rotated around a tilt axis and a series of 2D images is measured at different tilt angles (Fig. 1B). Due to geometric constraints, most samples cannot be tilted beyond ±79°, which is known as the missing wedge problem. One solution to this problem is to use needle-shaped specimens (*49*), allowing a full rotation around the axis of the needle. Another problem in STEM tomography is the electron beam damage to the specimen. This can be mitigated through a combination of approaches, including (i) choosing low operating voltages (such as 80 and 120 keV) to reduce the knock-on damage (*74*); (ii) using a dose-efficient STEM method (*75*), coupled with a direct electron detector (*37*); (iii) depositing a very thin layer of carbon film on the surface of the specimen (*44*); and (iv) implementing a low-exposure acquisition scheme—when acquiring an image at a tilt angle, a nearby sample is used to align and focus the image, thus reducing the unnecessary electron dose to the sample under study (*42*, *44*).

After the acquisition of an experimental tilt series, sample drift and scan distortion are corrected to minimize the experimental error (*49*). Advanced denoising techniques can also be applied to improve the image quality (*76*). The alignment of the tilt series is achieved by the center-of-mass method (*42*), which is based on the fact that the center of mass of a 3D object coincides with that of its projection images. By aligning all of the 2D images to the center of mass, a coarse alignment of the tilt series is accomplished. To achieve subangstrom precision, a fine alignment must be implemented by computing a 3D reconstruction from the coarse-aligned tilt series. The 3D reconstruction is back-projected to calculate a sequence of images at the corresponding experimental tilt angles. Quantitative comparison of the calculated and measured images allows fine-tuning of the alignment. This process is iterated until the alignment procedure converges.

Iterative algorithms for atomic tomographic reconstruction

To achieve atomic tomographic reconstruction, three issues associated with experimental tilt series must be addressed. First, the data are incomplete due to the missing wedge problem and because radiation damage limits the number of images. Second, there are experimental errors in the tilt series, such as small structure changes of the specimen during data acquisition, the mechanical tilt error of a sample stage, sample drift, and scanning distortion. Third, noise is present in every image. Although careful sample preparation, data acquisition, and denoising techniques can alleviate the experimental errors and reduce noise (*44*, *49*, *76*), iterative tomographic reconstruction algorithms are more suited to tackle the incomplete data issue than noniterative methods. Presently, there are two types of iterative algorithms for tomographic reconstruction. The first are real-space iterative algorithms, such as the algebraic reconstruction technique (ART), the simultaneous ART (SART), and the simultaneous iterative reconstruction technique (SIRT) (*77*–*79*). These algorithms compute a 3D reconstruction by iteratively solving a system of linear equations, in which positivity and mathematical regularization can be incorporated as constraints to reduce artifacts. Recently, SIRT has been applied to determine the 3D structure of a decahedral gold nanoparticle and a silver-gold nanocluster at atomic resolution (*50*, *51*).

The second type of algorithms iterates between real and Fourier space, an example being equal slope tomography (EST) (*80*–*84*), where the angles of a tomographic tilt series are spaced by equal slope instead of equal angle increments. The equal slope acquisition scheme allows the use of a variant of the fast Fourier transform (FFT), the pseudopolar FFT (PPFFT) (*85*). The PPFFT and its inverse are mathematically faithful and have a computing time comparable to that of the FFT. From an aligned tilt series, each image is inverted to a Fourier slice by a generalized Fourier transform called the fractional Fourier transform (Fig. 1C) (*86*). Using the inverse PPFFT, a 3D reconstruction is computed from this set of Fourier slices. Two general physical constraints are then applied to the reconstruction. First, a loose support (i.e., a 3D boundary larger than the shape of a specimen) is defined, and the intensity outside the support is set to zero. Next, any negative intensity inside the support is set to zero (positivity constraint), which produces a revised 3D reconstruction. The forward PPFFT is applied to the revised reconstruction, generating a full set of Fourier slices. The Fourier slices corresponding to the measured tilt angles are replaced with the experimental data, and the remaining slices are kept unchanged (Fig. 1C). This step produces a new full set of Fourier slices as an input for the next iteration. Progress is monitored by an error metric defined as the difference between the computed and measured slices at each iteration step, and the algorithm is terminated when no further improvement can be made (*80*–*84*). This entire process is then repeated using a tighter support, closer to the real shape of the object. After fine-tuning of the alignment with more iterations, a final 3D reconstruction is obtained. Through iterating between real and Fourier space, EST is gradually guided toward a best-possible solution that is concurrently consistent with the measured data and the general physical constraints. Quantitative comparison with experimental data indicates that EST produces 3D reconstructions with higher resolution, better contrast, and less distortion than real-space iterative algorithms such as ART and SART for a limited number of 2D images and a missing wedge (*81*). Furthermore, if needed, EST can also incorporate mathematical regularization

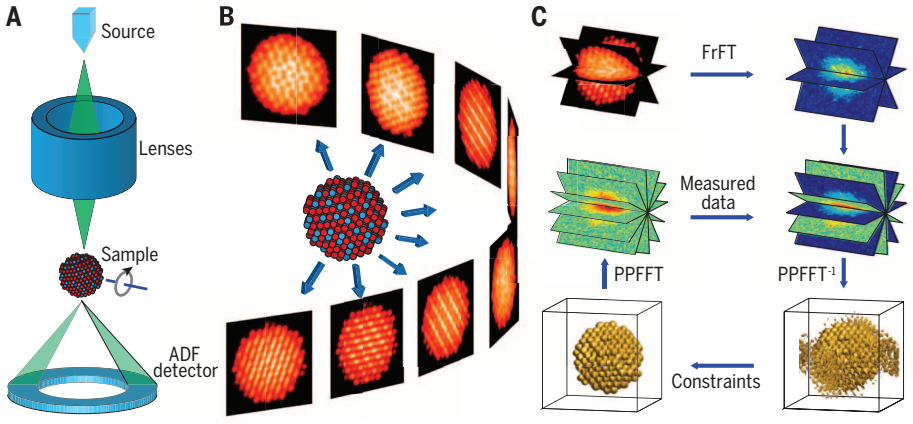

Fig. 1. Schematic layout of AET. (**A**) An electron beam is focused on a small spot and scanned over a sample to form a 2D image. The integrated signal at each scanning position is recorded by an ADF detector. (**B**) By rotating the sample around a tilt axis, a series of 2D images is measured at different tilt angles. (**C**) After preprocessing and alignment, the tilt series is inverted to Fourier slices by the fractional Fourier transform (FrFT). A 3D reconstruction is computed by using a Fourier-based iterative algorithm. From the 3D reconstruction, the coordinates of individual atoms are traced and refined to produce the 3D atomic model of the sample.

identical to real-space iterative algorithms (82–84). The drawback of EST is the requirement that the experimental tilt angles must be consistent with equal slope increments (80).

Two other methods have also been applied to AET through the incorporation of additional a priori constraints. By fitting atoms rigidly onto a crystal lattice, discrete tomography has been implemented to image the 3D atomic structure of a silver nanoparticle embedded in an aluminum matrix using only two high-angle ADF (HAADF)–STEM images (70). However, the crystallinity requirement limits the applicability of this approach, and the small number of images make this method sensitive to experimental errors and noise. A second approach is to reduce the input information needed through the use of compressed sensing electron tomography (87–89), which is based on the principle that a physically meaningful structure is usually sparse in some domain. If the sparse domain can be found, then the 3D structure can be reconstructed from a very small number of images (89). Compressed sensing electron tomography has been applied to image localized surface plasmon resonances of a silver nanocube (90) and to reach the atomic scale. By using only four or five HAADF-STEM images, the 3D structures of a gold nanorod and a core-shell Au@Ag nanorod have been imaged at atomic resolution (43, 45). However, it remains a challenge to find an appropriate sparse domain for each tomographic reconstruction. Furthermore, there are adjustable parameters in compressed sensing tomography, which vary for different samples. It is not straightforward to choose these parameters, especially with the presence of noise and experimental errors (89).

3D determination of the coordinates of individual atoms in materials

To probe material properties and functionality at the most fundamental scale, the 3D coordinates of individual atoms need to be determined from the 3D reconstruction, which can be accomplished using the following procedure (49). First, all local intensity maxima are identified from the 3D reconstruction and sorted from highest to lowest. Starting from the highest intensity, a 3D Gaussian function is fit to each peak. If a minimum distance between two neighboring atoms is satisfied, the peak of the Gaussian function is labeled as a candidate atom position, and the Gaussian function is subtracted from the 3D reconstruction. This step is repeated for all local maximum peaks. Second, a 3D atom profile is calculated by averaging the Gaussian functions of the most plausible atoms, excluding peaks with extremely high or low intensity. The Gaussian function of each candidate atom is quantitatively compared with the average atom profile. If the candidate atom matches more with the average atomic than the background, it is identified as an atom. This step produces a 3D atomic model. Third, a refinement procedure is implemented to improve the precision of the atom model using the measured images. Each measured image is Fourier transformed to produce a Fourier slice, and a corresponding Fourier slice is also calculated from a linear projection of the atomic coordinates. The positions of all atoms are iteratively refined by minimizing the difference between the measured and calculated Fourier slices. The refined atomic model is then compared with the 3D reconstruction, and a very small percentage of atoms are manually adjusted to ensure that they are consistent with the reconstructed intensity and the local stereochemistry of the material (41). An updated atomic model is obtained and refined once again with the measured data. This step is repeated until no further improvements can be made. Fourth, to verify the final atomic model, 2D images are calculated from the atomic coordinates using multislice simulations with the same experimental parameters (91). After adding noise, the calculated images should agree well with the measured ones. Furthermore, by using the same reconstruction, atomic tracing, and refinement procedures, a new 3D atomic model can be computed from the noisy multislice images. This model must be consistent with the final model; otherwise, the whole atom tracing and refinement process must be redone to obtain a final model. Although the procedures described here focus on samples with a single atomic species, they can, in principle, be extended to determine the coordinates of multiple atomic species in materials based on the Z-contrast of STEM images (46).

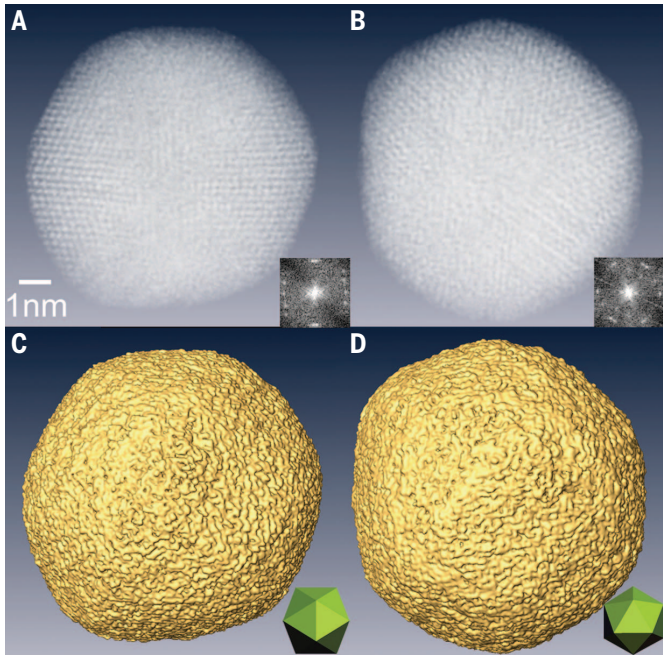

Fig. 2. Experimental demonstration of AET without assuming crystallinity or using averaging. (**A** and **B**) Volume renderings of the 3D reconstruction of a gold nanoparticle and their Fourier transforms (insets) along the two- and threefold symmetry directions, respectively. Individual atoms are visible in the reconstruction, and several major 3D grains are identified at atomic-scale resolution. (**C** and **D**) Surface renderings of the 3D reconstruction along the two- and threefold symmetry directions, respectively, indicating that this is a multiply twinned icosahedral nanoparticle. The insets show an icosahedron model along the same symmetry directions. [From (42)]

Single-particle reconstruction: From 3D structure determination of macromolecules to small metal nanoparticles at atomic-scale resolution

Single-particle cryo-EM has become a very important method for 3D structure determination of macromolecules at near-atomic resolution (33–37). High-resolution imaging of biological materials at room temperature is difficult in the transmission electron microscope due to electron beam damage and the low scattering contrast of light atoms such as carbon (32). Plunge freezing of buffered aqueous solutions to produce vitreous ice containing purified biological molecules was developed to prepare the structure for imaging in their native hydrated state (28). Noisy projection images of individual molecules with identical or similar conformations can be acquired at very low doses (20 to 40 electrons per Å^2). Traditionally, hundreds of thousands to millions of such images are first classified, averaged, and then oriented in 3D space to produce a tomographic reconstruction of the molecule (33). Until recently, the resolution of this technique was generally limited to >4 Å because the extremely low doses resulted in noisy images with poor contrast (33). High-resolution structures have only become achievable with the development of the direct electron detector, resulting in a revolution in cryo-EM with near atomic (<4 Å) resolution (34–37). The direct electron detector provides substantially better quantum efficiency, point spread function, and acquisition speed than a traditional scintillator paired with a charge-coupled device, allowing the accurate determination of the position of individual electron strikes (38). Rapidly acquired images can also be aligned and averaged to high accuracy to remove sample drift and beam-induced motion during acquisition (92). Furthermore, through a combination of statistical approach and prior knowledge, advanced 3D reconstruction algorithms have been developed to extract as much structure information as possible from very noisy cryo-EM data (39, 40).

Single-particle 3D reconstruction developed for cryo-EM has also been applied to image small (≤2 nm) metal clusters at atomic-scale resolution.

Homogeneous gold clusters consisting of 68 atoms were imaged at random orientations with an aberration-corrected TEM. These 2D images were then combined to determine the 3D atomic structure of the gold cluster (*47*). In situ TEM was also coupled with a fast-acquisition direct electron detector to image platinum nanocrystals freely rotating in a graphene liquid cell. By acquiring many images at different orientations, the 3D structure of individual heterogeneous nanocrystals was determined at near-atomic resolution (*48*). In addition to single-particle 3D reconstruction, TEM-based methods have also been demonstrated to determine the 3D atomic positions of two-layer graphene (*93*) utilizing the curvature of the scattered electron wave (*94*) and the 3D atomic morphology of a thin MgO crystal (*95*), each of which was achieved from a single sample orientation.

Interdisciplinary science enabled by AET

3D imaging of crystal defects in materials at atomic resolution

Crystal defects such as point defects, dislocations, grain boundaries, and stacking faults strongly influence material properties and are crucial to materials engineering (*1*–*3*). Although a number of experimental methods have been used to image crystal defects since the 1950s (*12*, *96*–*99*), 3D imaging of the atomic arrangements in the cores of dislocations, grain boundaries, and stacking faults has only recently become possible through the use of AET. By combining ADF-STEM with EST, AET was first demonstrated to image a gold nanoparticle at 2.4 Å resolution without assuming crystallinity or using averaging (*42*). Figure 2, A to D, shows volume and iso-surface renderings of the 3D reconstruction, indicating that this is a multiply-twinned icosahedral nanoparticle. Individual atoms are visible in the reconstruction, and several major 3D grains are identified at atomic-scale resolution.

To probe crystal defects at higher resolution and contrast, AET was applied to image the 3D structure of a platinum nanoparticle from a large number of STEM images (*44*). Due to the weak signal from individual atoms, 3D Fourier filtering was used to enhance the signal-to-noise ratio of the reconstruction. As this may potentially introduce artifacts (*100*, *101*), two independent approaches were implemented to verify the results of using the Fourier filtering. First, multislice STEM calculations were combined with EST to examine and optimize the filtering parameters while avoiding artifacts. Second, well-established Wiener filtering was used to corroborate the experimental results (*102*). Figure 3, A and B, shows the grain boundaries of the platinum nanoparticle after independent filtering verification. A measured 2D image suggests that this is a multiply twinned decahedral nanoparticle with flat twin boundaries (Fig. 3A).

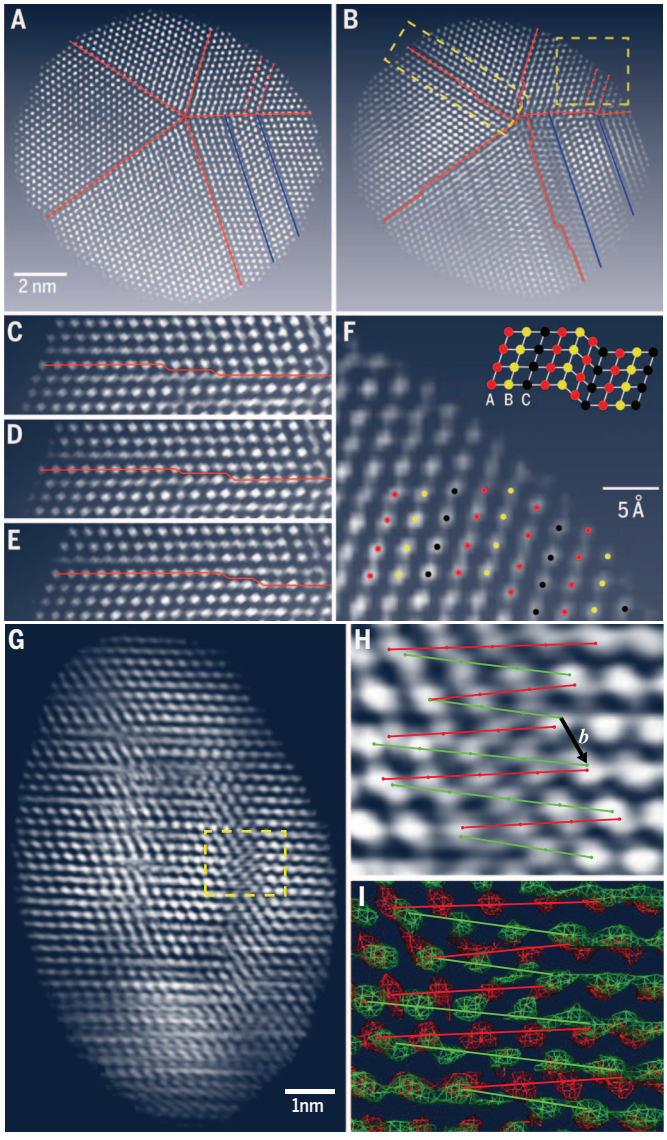

Fig. 3. 3D imaging of crystal defects in materials at atomic resolution. (**A**) STEM image of a decahedral platinum nanoparticle, showing flat twin boundaries. (**B**) A 2.6 Å thick internal atomic layer of the nanoparticle reconstructed by AET, revealing that the twin boundaries are not flat but instead form atomic steps. Boxed areas indicate a grain boundary and a stacking fault. (**C**) Enlarged view of the grain boundary in (B). (**D** and **E**) A 2.6 Å thick atomic layer above and below the layer shown in (C). The three consecutive internal atomic layers further confirm that the atomic steps continuously vary along the consecutive layers. (**F**) Enlarged view of the 2.6 Å thick stacking fault in (B), which ends at a twin boundary. The inset shows a classical model of an fcc extrinsic stacking fault. (**G**) A 5.3 Å thick internal slice (two atomic layers) of the nanoparticle reconstructed by AET. (**H** and **I**) 3D volume and surface renderings of an enlarged view of the core of a screw dislocation in (G) with the Burgers vector (**b**) of $\frac{1}{2}[01\bar{1}]$. [From (*44*)].

However, an internal atomic layer reveals that the twin boundaries are not flat but instead form atomic steps (Fig. 3B). Three consecutive internal atomic layers further confirm that the atomic steps continuously vary along the consecutive atomic layers (Fig. 3, C to E). Figure 3B also shows that the subgrain boundaries in an internal atomic layer are slightly widened relative to those in the 2D image (Fig. 3A). In relation to the grain boundary, a stacking fault is also observed at the single-atom level (Fig. 3F), which ends at a twin boundary (Fig. 3B). Furthermore, from the 3D reconstruction of the platinum nanoparticle, the 3D core structure of both edge and screw dislocations are imaged at atomic resolution (*44*). Figure 3G shows a 5.3 Å thick internal slice of the nanoparticle, and a zigzag pattern, a characteristic feature of a screw dislocation core, is visible in the enlarged views (Fig. 3, H and I). The Burgers vector of the screw dislocation was measured to be $\frac{1}{2}[01\bar{1}]$. Careful examination of the locations of the screw dislocation and the atomic steps at the twin boundary indicates that they are associated with a strain relaxation mechanism for the multiply twinned decahedral nanoparticle (*44*). These results indicate that AET is crucial to probing crystal defects in materials as 2D projection images may sometimes provide deceptive structural information.

3D measurements of the atomic displacements and the full strain tensor in materials

The structural, mechanical, electronic, and optical properties of many materials are directly related to the strain in the materials (*1*, *2*, *103*). However, conventional methods to measure local strain at the nanoscale, using TEM, electron diffraction, and holography, are limited to 2D (*103*–*105*). Although coherent diffractive imaging, x-ray diffraction microscopy, and through-focal ADF imaging can measure the strain tensor in 3D (*17*, *19*, *106*, *107*), they offer limited spatial resolution. Recently, the 3D strain field in a gold nanorod was imaged at high resolution using compressed sensing electron tomography (*43*). However, because this method used four STEM images, only one of the six components of the strain tensor (ε_{zzz}) was measured. In order to determine the full strain tensor in materials with high precision and spatial resolution, a method must be able to precisely localize the coordinates of individual atoms without assuming crystallinity.

AET was recently used to determine the 3D positions of individual atoms in a tungsten needle sample (*49*). A tilt series of 62 images was measured with an aberration-corrected ADF-STEM. By combining EST with 3D atom tracing and refinement procedures, the coordinates of 3769 individual atoms of the needle apex were determined with a precision of about 10.5, 15, and 5.5 pm along the *x*, *y*, and *z* axes, respectively (i.e., ~19 pm in three dimensions) (Fig. 4A) (*49*). The ability to precisely localize the individual atom positions with AET is attributed to minimizing the dynamical scattering effect by avoiding the exact zone axes and measuring many images at different sample orientations (i.e., a rotational average), which is analogous to the reduction of dynamical effects in precession electron diffraction (*108*). Furthermore, a point defect is identified in the 3D reconstruction with high precision (*49*). Figure 4, B and C, shows the reconstructed intensity and its surface rendering surrounding a point defect in layer six, indicating that there is no tungsten atom in the defect site. Although field ion microscopy has been applied to obtain 3D information of atoms and vacancies in needle-shaped specimens with a priori assumptions and low precision (*109*, *110*), 3D identification and localization of point defects in materials at high precision without any prior knowledge has been considered to be one of the ultimate goals in materials characterization.

By comparing the coordinates of individual atoms (Fig. 4D) with an ideal tungsten crystal lattice, the atomic displacement field and the strain tensor were determined in three dimensions (*49*). As the strain measurements require differentiation of the displacement field and are sensitive to noise, a 5.5 Å wide 3D Gaussian kernel was convolved with the displacement field to enhance the signal-to-noise ratio and precision. Figure 4, E to G, shows the 3D atomic displacements of the tungsten needle sample, exhibiting expansion in the $[0\bar{1}1]$ direction (*x* axis) and compression in the [100] direction (*y* axis). The atomic displacements along the [001] direction (*z* axis) are much smaller than those in the *x* and *y* axes. The six components of the strain tensor (ε_{xx}, ε_{yy}, ε_{zz}, ε_{xy}, ε_{xz}, and ε_{yz}) were obtained from the convolved displacement field with a 3D resolution of 1 nm and a precision of 10^{-3} (Fig. 4, H to M). The ε_{xx} and ε_{yy} maps show features related to the lattice expansion and compression along the *x* and *y* axes, respectively, while the ε_{zz} component is smaller and smoother. Shear in the *xy*, *xz*, and *yz* planes is observed in the ε_{xy}, ε_{xz}, and ε_{yz} maps. The principal strains were determined to be 0.81%, −0.87%, and −0.15% along the [0.074 0.775 −0.628], [0.997 −0.083 0.015], and [0.041 0.627 0.778] directions, respectively. Further experimental, density functional theory (DFT), and molecular dynamics results have confirmed that the strain was induced by surface tungsten carbide and the diffusion of carbon atoms below the tungsten surface (*49*). As conventional methods for strain measurements are primarily based on geometric-phase analysis of crystalline samples in Fourier space (*103*, *104*), the ability to precisely determine the 3D positions of individual atoms opens the door toward directly measuring the strain tensor in materials at the atomic scale (*49*–*51*).

3D structure determination of ligand-protected gold nanoparticles at atomic resolution

Ligand-protected gold nanoparticles on the order of 1 to 2 nm in diameter exhibit different electronic and optical properties from bulk materials and are expected to find broad applications in several disciplines (*111*). However, these water-soluble nanoparticles are difficult to crystallize, and only a small number of structures have been solved by x-ray crystallography (*112*). Single-particle 3D reconstruction was recently applied to determine the structure of ligand-protected Au nanoparticles at atomic resolution (*47*). In this experiment, 939 aberration-corrected TEM images of homogeneous 68-gold-atom nanoparticles (Au_{68}NPs) were used to reconstruct the 3D structure. Figure 5A shows the reconstructed intensity and the positions of all 68 gold atoms. The 3D atomic model of the Au_{68}NP reveals that a gold atom at the center is surrounded by a cagelike cuboctahedron of 12 atoms. Twenty-four additional atoms form a face-centered cubic (fcc)–like shell around the cuboctahedron, whereas the remaining 31 atoms deviate from fcc packing (Fig. 5B). Because the surface ligand molecules and sulfur atoms cannot be measured by this method, 32 sulfur atoms were manually added to

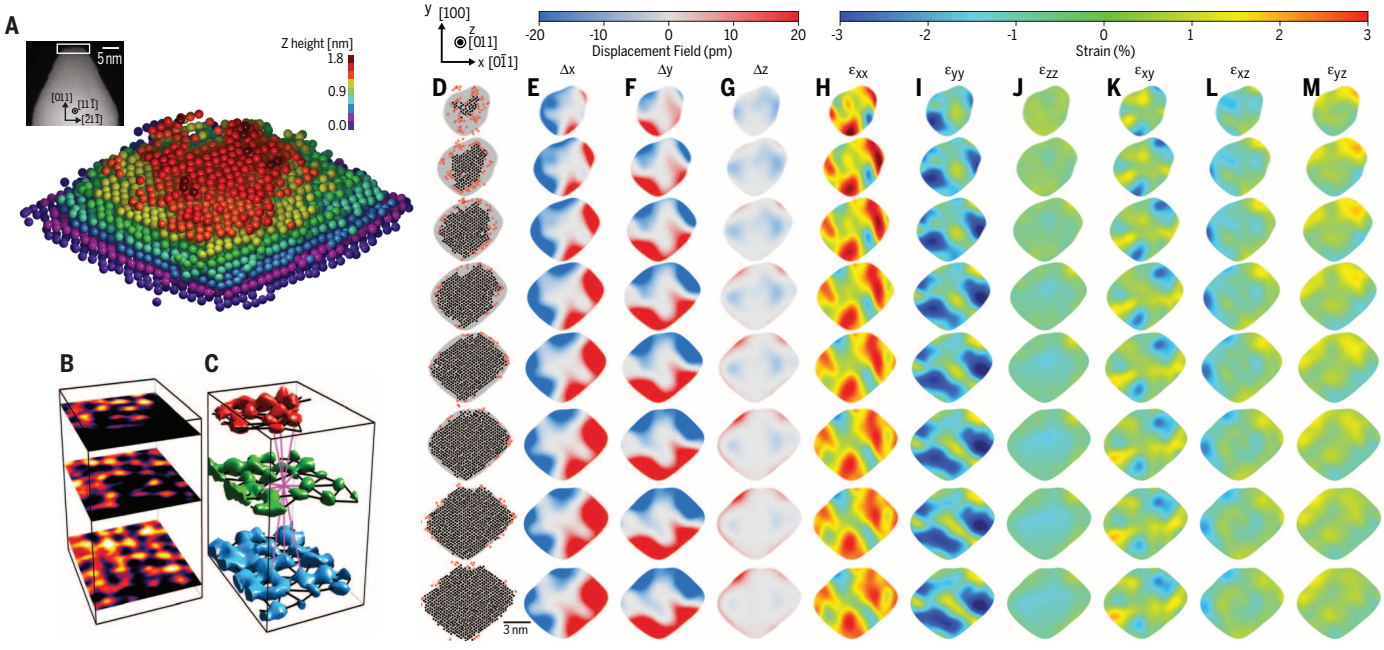

Fig. 4. 3D measurements of individual atom coordinates, atomic displacements, and the strain tensor in materials. (**A**) Coordinates of 3769 individual atoms determined from the top nine layers of a tungsten needle sample (inset) with a 3D precision of ~19 pm. Layers one to nine are shown in dark red, red, orange, yellow, green, cyan, blue, magenta, and purple, respectively. (**B** and **C**) 3D reconstructed intensity and its surface rendering surrounding a point defect in layer six of the needle sample. (**D**) Individual atoms in layers two to nine of the tungsten needle sample used to determine the atomic displacements and the strain tensor. Layer one and some surface atoms in red were excluded due to their large deviation from an ideal body-centered cubic lattice. (**E** to **G**) 3D atomic displacements of the needle sample, exhibiting expansion in the $[0\bar{1}1]$ direction (*x* axis) and compression in the [100] direction (*y* axis). (**H** to **M**) The ε_{xx}, ε_{yy}, ε_{zz}, ε_{xy}, ε_{xz}, and ε_{yz} components of the strain tensor. The ε_{xx} and ε_{yy} components exhibit features directly related to the lattice expansion and compression along the *x* and *y* axes, respectively. Shear in the *xy*, *xz*, and *yz* planes is visible in the ε_{xy}, ε_{xz}, and ε_{yz} maps, respectively. [From (*49*)]

the final model based on the positions of the gold atoms and the local stereochemistry (Fig. 5C). DFT calculations were used to relax the final atomic model to a local minimum energy, confirming that the positions of most gold atoms remain the same (Fig. 5D) (*47*, *113*). Several surface atoms deviate from measured positions, probably because of hydrogen bonding between surface ligands. The 3D atomic model of Au_{68}NP determined from this experiment exhibits lower symmetry than that of Au_{102}NP and is also different from the theoretical prediction of the highly symmetrical atomic structure of a similar nanoparticle, $Au_{67}(SR)_{35}$. This work shows that single-particle 3D reconstruction can be used to determine the atomic structure of small (≤2 nm) and homogeneous metal nanoparticles that are difficult to crystallize. To achieve a full 3D reconstruction of both the highly scattering and lightly scattering atoms (such as ligand molecules), further improvements could involve the use of direct electron detectors to improve the signal-to-noise ratio and reduce the radiation dose (*38*). Also, imaging of frozen hydrated samples in vitreous ice could provide the structure of the nanoparticles in their native solvated state (*33*).

3D structure of individual heterogeneous nanoparticles in solution at near-atomic resolution

In situ liquid cell using graphene offers the opportunity to image single objects at atomic resolution under dynamic conditions (*114*). It was noticed that the objects are randomly rotating in solution, providing many different views that could be used in electron tomography. This led to the development of 3D structure determination of heterogeneous nanoparticles at near-atomic resolution using the single-nanoparticle reconstruction method (*48*). In this first experiment, platinum nanoparticles were chosen for their high scattering signals and scientific importance in catalysis applications. Two sheets of graphene were used to contain a solution of the nanocrystals within the vacuum of an aberration-corrected TEM. A fast acquisition direct electron detector was used to rapidly acquire many images of the nanoparticles freely rotating in solution (*38*). An ab initio single-particle reconstruction approach was used to determine projection orientations stochastically without fitting to an a priori model (*115*), thus avoiding model bias. The final reconstructions of two individual ~2-nm diameter platinum nanoparticles reach near-atomic resolution (Fig. 6).

Figure 6, A and B, shows the 3D reconstruction of two nanoparticles and the cross-sectional views along the vertical plane, respectively. The overall nonsymmetric structures of the two nanoparticles are similar and described as a central disc of {111} atomic planes with two conical crystalline protrusions attached by screw dislocations on either end of the disc (Fig. 6C) (*48*). The observation of screw dislocations in platinum nanoparticles independently confirms the earlier AET results (*44*), suggesting that the 3D atomic structure of nanoparticles is more complex than previously thought. Figure 6D shows the 3D structure of the nanoparticles viewed along the conical protrusion direction. The crystalline lattices of the protrusion (Fig. 6D) and the core (Fig. 6E) form a tilt angle of 14° for particle one and 7° for particle two (Fig. 6F). Additional differences between the two structures of the nanoparticles include surface morphology and the degree of crystallinity in each domain. Calculations of the exposed-surface free energy and grain-boundary free energy indicate a strong driving force for coalescence and support that the orientation of the side protrusions with respect to the central section are the minimum energy of the system.

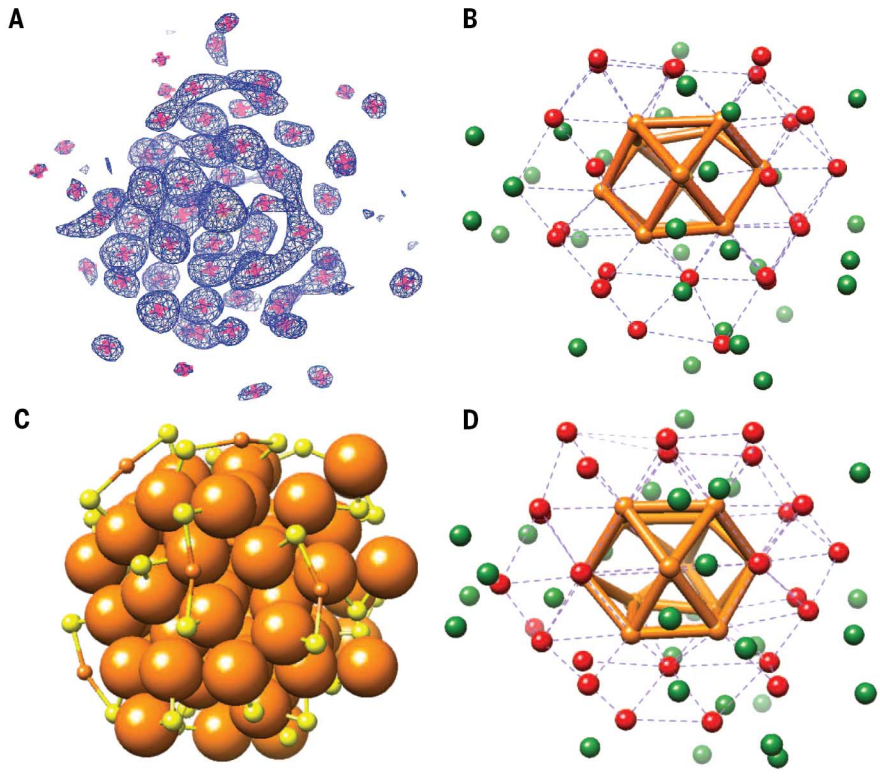

Fig. 5. 3D structure determination of ligand-protected gold nanoparticles at atomic resolution. (**A**) 3D intensity and positions of 68 gold atoms reconstructed from 939 Au_{68}NPs using the single-particle method. (**B**) 3D atomic model of Au_{68}NP. A gold atom at the center is surrounded by a cagelike cuboctahedron of 12 atoms (orange). Twenty-four additional atoms (red) form a fcc-like shell around the cuboctahedron, whereas the remaining 31 atoms (green) deviate from fcc packing. (**C**) 3D atomic model of $Au_{68}(SH)_{32}$. Thirty-two sulfur atoms (yellow) were manually added to the final model based on the positions of the gold atoms (orange) and the local stereochemistry. Gold atoms outside the Au_{15} fcc core are labeled with smaller spheres to better show Au-S motifs. (**D**) The Au_{68} atomic model from DFT calculations, confirming that the positions of most gold atoms are consistent with those of the measured model shown in (B). Several surface atoms deviate from measured positions, probably due to hydrogen bonding between surface ligands. [From (*47*)]

Looking forward

Although x-ray crystallography has been the primary method of solving the 3D atomic structure of crystals over the last century, the ability to determine the 3D structure of crystal defects and noncrystalline systems at atomic resolution will transform our understanding of materials properties and functionality at the most fundamental level. Here we identify five future research frontiers enabled by AET. First, 3D localization and identification of all atomic species in complex systems (including dopants, interstitials, light elements, and vacancies) require the further developments of AET. New STEM imaging methods such as matched illumination and detector interferometry can be implemented to image simultaneously heavy and light elements (*75*). Advanced image reconstruction and atom-tracing algorithms must be further improved to precisely localize the 3D atomic positions of individual light elements such as C and O, based on the intensity of reconstructed peaks. The measured atomic positions can then be used by DFT to obtain the 3D electronic properties of these complex systems at the single-atom level (*116*). Furthermore, AET may be combined with electron energy loss spectroscopy to directly measure the electronic states of these systems and verify the DFT results (*117*). Second, surfaces and interfaces strongly influence the catalytic, electronic, magnetic, and optical properties of many materials (*118*). Although x-ray, electron, and neutron diffraction and scanning probe microscopes have been successfully applied to investigate the atomic and electronic structure of surfaces and interfaces (*118*), AET is specifically suited

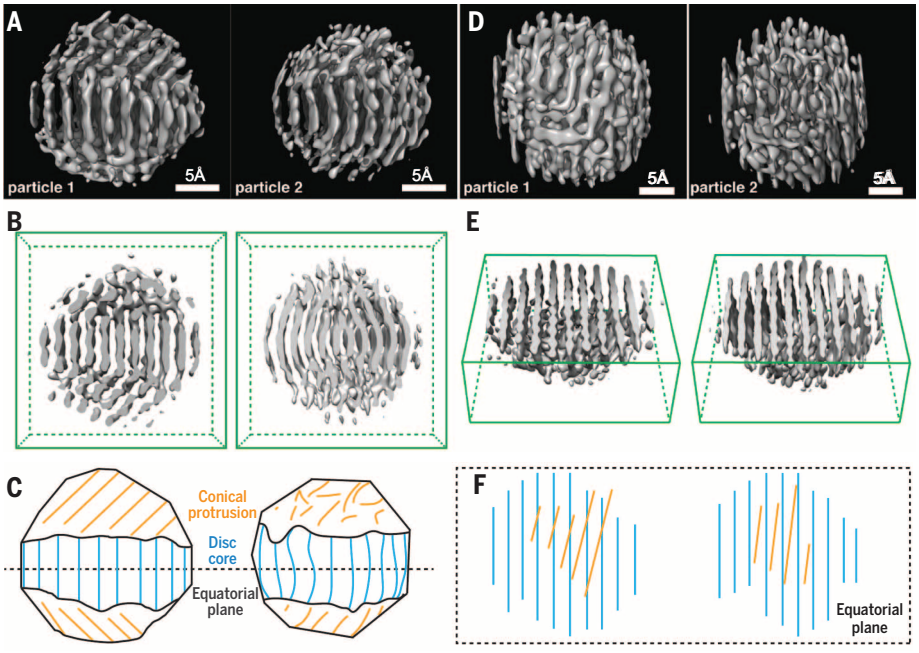

Fig. 6. 3D imaging of individual heterogeneous nanoparticles in solution at near-atomic resolution. (**A**) 3D structure of two platinum nanoparticles in liquid reconstructed by the single-particle method. (**B**) Cross-sectional views of the two 3D structures along the vertical plane of (A). (**C**) Schematic illustration of the atomic planes in the nanoparticles viewed at the same orientation as in (A). The overall structure of each nanoparticle consists of a central disc of {111} planes (blue) with two attached conical protrusions (yellow). (**D**) 3D structure of the two nanoparticles viewed along the conical protrusion direction. (**E**) Cross-sectional views of the two 3D structures along the equatorial plane shown in (C). (**F**) Schematic illustration of the nanoparticles viewed along the conical protrusion direction, showing that the lattice of the core (blue lines) and protrusions (yellow lines) form a tilt angle of 14° for particle one and 7° for particle two. [From (*48*)]

to precise probing of the 3D positions of individual atoms of many important systems, including the surface and subsurface atomic structure of heterogeneous catalysts, as well as metal-semiconductor, metal-oxide, and crystal-amorphous interfaces. Achieving these challenging goals will require sophisticated sample preparation, state-of-the-art electron microscopes equipped with advanced detectors, new STEM imaging methods with reduced electron doses, advanced tomographic reconstruction, and atom-tracing algorithms. In addition, many interfaces are extended in two dimensions, and determining the 3D arrangement of extended objects requires the further improvement of the reconstruction algorithm. Third, amorphous materials such as glasses are ubiquitous in our daily life, but the 3D atomic structure of glasses and other amorphous materials has thus far defied any direct experimental determination due to its lack of long-range translational and orientational order (*4*, *119*). Through a combination of multislice simulations of an aberration-corrected STEM and EST, the 3D atomic structure of a simulated glass particle was reconstructed from a tilt series of 55 noisy images, from which the 3D positions of individual Si and O atoms were identified (*46*). These numerical results indicate the feasibility of applying AET to determine the 3D atomic structure of amorphous materials. Likewise, AET can, in principle, be used to resolve the 3D atomic positions and species in quasicrystals (*120*, *121*). Fourth, an ultimate challenge is to develop AET for probing the dynamics of individual atoms and defects in materials (*122*). For example, understanding the 3D motion and interaction of point defects, dislocations, and grain boundaries at atomic resolution remains a long-standing unresolved problem in materials science. Likewise, monitoring the motion of individual atoms in complex systems during phase transitions or under external mechanical stress is beyond the capability of any existing experimental techniques (*5*). Addressing these challenging problems demands far more advanced electron microscopes and tomographic reconstruction methods than currently exist.

Finally, we note that small particles are rarely used individually in applications. Real devices consist of multiscale heterogeneous assemblies of materials that work together to yield the desired functionality. To study materials in action, we desire experimental methods that can carry out in situ or operando studies of local structure from actual devices (*123*–*126*). Enormous progress has been made in this endeavor through the use of so-called total scattering methods, such as the atomic pair distribution function method that scatters x-rays, neutrons, or electrons from ensembles of fine-grained and nanosized materials (*127*). Total scattering allows movies to be made showing how functional materials change under load (for example, by following structural changes in a battery electrode during discharge, or in an operating fuel cell). But averaging, as the measurements do, over many particles and particle orientations, results in considerable information loss in the signal and a fuzzy, nonunique picture of what is occurring in the material (*128*, *129*). Combining detailed structures from AET with total scattering approaches holds the transformational promise of giving us truly robust models of complex, heterogeneous materials in action; helping us to understand why high-performance materials work so well; and providing insights into how to design better ones (*130*, *131*).

REFERENCES AND NOTES

1. A. A. Kelly, K. M. Knowles, *Crystallography and Crystal Defects* (Wiley, ed. 2, 2012).
2. D. J. Bacon, D. Hull, Eds., *Introduction to Dislocations* (Butterworth-Heinemann, ed. 5, 2011).
3. M. D. McCluskey, E. E. Haller, *Dopants and Defects in Semiconductors* (CRC Press, 2012).
4. R. Zallen, *The Physics of Amorphous Solids* (Wiley, 1998).
5. P. G. Debenedetti, F. H. Stillinger, Supercooled liquids and the glass transition. *Nature* **410**, 259–267 (2001). doi: 10.1038/35065704; pmid: 11258381
6. H. W. Sheng, W. K. Luo, F. M. Alamgir, J. M. Bai, E. Ma, Atomic packing and short-to-medium-range order in metallic glasses. *Nature* **439**, 419–425 (2006). doi: 10.1038/nature04421; pmid: 16437105
7. J. M. Thomas, W. J. Thomas, *Principles and Practice of Heterogeneous Catalysis* (Wiley, ed. 2, 2014).
8. M. A. Green, K. Emery, Y. Hishikawa, W. Warta, E. D. Dunlop, Solar cell efficiency tables (version 45). *Prog. Photovolt. Res. Appl.* **23**, 1–9 (2015). doi: 10.1002/pip.2573
9. A. S. Aricò, P. Bruce, B. Scrosati, J.-M. Tarascon, W. van Schalkwijk, Nanostructured materials for advanced energy conversion and storage devices. *Nat. Mater.* **4**, 366–377 (2005). doi: 10.1038/nmat1368; pmid: 15867920
10. J. Senior, *Optical Fiber Communications: Principles and Practice* (Pearson, ed. 3, 2008).
11. M. Wuttig, N. Yamada, Phase-change materials for rewriteable data storage. *Nat. Mater.* **6**, 824–832 (2007). doi: 10.1038/nmat2009; pmid: 17972937
12. P. Hirsch, D. Cockayne, J. Spence, M. Whelan, 50 Years of TEM of dislocations: Past, present and future. *Philos. Mag.* **86**, 4519–4528 (2006). doi: 10.1080/14786430600768634
13. D. B. Williams, C. B. Carter, *Transmission Electron Microscopy: A Textbook for Materials Science* (Springer, ed. 2, 2009).
14. J. C. H. Spence, *Experimental High-Resolution Electron Microscopy* (Oxford Univ. Press, ed. 3, 2003).
15. B. Bhushan, O. Marti, in *Springer Handbook of Nanotechnology*, P. B. Bhushan, Ed. (Springer, 2010), pp. 573–617.
16. J. Miao, P. Charalambous, J. Kirz, D. Sayre, Extending the methodology of x-ray crystallography to allow imaging of micrometre-sized non-crystalline specimens. *Nature* **400**, 342–344 (1999). doi: 10.1038/22498
17. I. Robinson, R. Harder, Coherent x-ray diffraction imaging of strain at the nanoscale. *Nat. Mater.* **8**, 291–298 (2009). doi: 10.1038/nmat2400; pmid: 19308088
18. J. Miao, T. Ishikawa, I. K. Robinson, M. M. Murnane, Beyond crystallography: Diffractive imaging using coherent x-ray light sources. *Science* **348**, 530–535 (2015). doi: 10.1126/science.aaa1394; pmid: 25931551
19. J. Miao, T. Ohsuna, O. Terasaki, K. O. Hodgson, M. A. O'Keefe, Atomic resolution three-dimensional electron diffraction microscopy. *Phys. Rev. Lett.* **89**, 155502 (2002). doi: 10.1103/PhysRevLett.89.155502; pmid: 12365999
20. J. M. Zuo, I. Vartanyants, M. Gao, R. Zhang, L. A. Nagahara, Atomic resolution imaging of a carbon nanotube from diffraction intensities. *Science* **300**, 1419–1421 (2003). doi: 10.1126/science.1083887; pmid: 12775837
21. W. J. Huang *et al.*, Coordination-dependent surface atomic contraction in nanocrystals revealed by coherent diffraction. *Nat. Mater.* **7**, 308–313 (2008). doi: 10.1038/nmat2132; pmid: 18327263

22. K. Ayyer *et al.*, Macromolecular diffractive imaging using imperfect crystals. *Nature* **530**, 202–206 (2016). doi: 10.1038/nature16949; pmid: 26863980
23. T. F. Kelly, M. K. Miller, Atom probe tomography. *Rev. Sci. Instrum.* **78**, 031101 (2007). doi: 10.1063/1.2709758; pmid: 17411171
24. M. P. Moody *et al.*, Atomically resolved tomography to directly inform simulations for structure-property relationships. *Nat. Commun.* **5**, 5501 (2014). doi: 10.1038/ncomms6501; pmid: 25407499
25. D. J. De Rosier, A. Klug, Reconstruction of three dimensional structures from electron micrographs. *Nature* **217**, 130–134 (1968). doi: 10.1038/217130a0; pmid: 23610788
26. W. Hoppe, R. Langer, G. Knesch, C. Poppe, Protein-Kristallstrukturanalyse mit Elektronenstrahlen. *Naturwissenschaften* **55**, 333 (1968). doi: 10.1007/BF00600449; pmid: 5700719
27. R. G. Hart, Electron microscopy of unstained biological material: The polytropic montage. *Science* **159**, 1464–1467 (1968). doi: 10.1126/science.159.3822.1464; pmid: 4183952
28. J. Dubochet *et al.*, Cryo-electron microscopy of vitrified specimens. *Q. Rev. Biophys.* **21**, 129–228 (1988). doi: 10.1017/S0033583500004297; pmid: 3043536
29. J. Frank, *Electron Tomography: Methods for Three-Dimensional Visualization of Structures in the Cell* (Springer, 2010).
30. V. Lučić, F. Förster, W. Baumeister, Structural studies by electron tomography: From cells to molecules. *Annu. Rev. Biochem.* **74**, 833–865 (2005). doi: 10.1146/annurev.biochem.73.011303.074112; pmid: 15952904
31. C. M. Oikonomou, G. J. Jensen, A new view into prokaryotic cell biology from electron cryotomography. *Nat. Rev. Microbiol.* **14**, 205–220 (2016). doi: 10.1038/nrmicro.2016.7; pmid: 26923112
32. R. Henderson, The potential and limitations of neutrons, electrons and x-rays for atomic resolution microscopy of unstained biological molecules. *Q. Rev. Biophys.* **28**, 171–193 (1995). doi: 10.1017/S003358350000305X; pmid: 7568675
33. J. Frank, *Three-Dimensional Electron Microscopy of Macromolecular Assemblies: Visualization of Biological Molecules in Their Native State* (Oxford Univ. Press, 2006).
34. E. Callaway, The revolution will not be crystallized: A new method sweeps through structural biology. *Nature* **525**, 172–174 (2015). doi: 10.1038/525172a; pmid: 26354465
35. Y. Cheng, Single-particle cryo-EM at crystallographic resolution. *Cell* **161**, 450–457 (2015). doi: 10.1016/j.cell.2015.03.049; pmid: 25910205
36. E. Nogales, The development of cryo-EM into a mainstream structural biology technique. *Nat. Methods* **13**, 24–27 (2016). doi: 10.1038/nmeth.3694; pmid: 27110629
37. A. Bartesaghi *et al.*, 2.2 Å resolution cryo-EM structure of β-galactosidase in complex with a cell-permeant inhibitor. *Science* **348**, 1147–1151 (2015). doi: 10.1126/science.aab1576; pmid: 25953817
38. M. Battaglia, D. Contarato, P. Denes, P. Giubilato, Cluster imaging with a direct detection CMOS pixel sensor in transmission electron microscopy. *Nucl. Instrum. Methods* **608**, 363–365 (2009). doi: 10.1016/j.nima.2009.07.017
39. S. H. W. Scheres, RELION: Implementation of a Bayesian approach to cryo-EM structure determination. *J. Struct. Biol.* **180**, 519–530 (2012). doi: 10.1016/j.jsb.2012.09.006; pmid: 23000701
40. D. Lyumkis, A. F. Brilot, D. L. Theobald, N. Grigorieff, Likelihood-based classification of cryo-EM images using FREALIGN. *J. Struct. Biol.* **183**, 377–388 (2013). doi: 10.1016/j.jsb.2013.07.005; pmid: 23872434
41. A. T. Brünger *et al.*, Crystallography & NMR system: A new software suite for macromolecular structure determination. *Acta Crystallogr. D* **54**, 905–921 (1998). doi: 10.1107/S0907444998003254; pmid: 9757107
42. M. C. Scott *et al.*, Electron tomography at 2.4-ångström resolution. *Nature* **483**, 444–447 (2012). doi: 10.1038/nature10934; pmid: 22437612
43. B. Goris *et al.*, Atomic-scale determination of surface facets in gold nanorods. *Nat. Mater.* **11**, 930–935 (2012). doi: 10.1038/nmat3462; pmid: 23085569
44. C.-C. Chen *et al.*, Three-dimensional imaging of dislocations in a nanoparticle at atomic resolution. *Nature* **496**, 74–77 (2013). doi: 10.1038/nature12009; pmid: 23535594
45. B. Goris *et al.*, Three-dimensional elemental mapping at the atomic scale in bimetallic nanocrystals. *Nano Lett.* **13**, 4236–4241 (2013). doi: 10.1021/nl401945b; pmid: 23952010
46. C. Zhu *et al.*, Towards three-dimensional structural determination of amorphous materials at atomic resolution. *Phys. Rev. B* **88**, 100201 (2013). doi: 10.1103/PhysRevB.88.100201
47. M. Azubel *et al.*, Electron microscopy of gold nanoparticles at atomic resolution. *Science* **345**, 909–912 (2014). doi: 10.1126/science.1251959; pmid: 25146285
48. J. Park *et al.*, 3D structure of individual nanocrystals in solution by electron microscopy. *Science* **349**, 290–295 (2015). doi: 10.1126/science.aab1343; pmid: 26185247
49. R. Xu *et al.*, Three-dimensional coordinates of individual atoms in materials revealed by electron tomography. *Nat. Mater.* **14**, 1099–1103 (2015). doi: 10.1038/nmat4426; pmid: 26390325
50. B. Goris *et al.*, Measuring lattice strain in three dimensions through electron microscopy. *Nano Lett.* **15**, 6996–7001 (2015). doi: 10.1021/acs.nanolett.5b03008; pmid: 26340328
51. G. Haberfehlner *et al.*, Formation of bimetallic clusters in superfluid helium nanodroplets analysed by atomic resolution electron tomography. *Nat. Commun.* **6**, 8779 (2015). doi: 10.1038/ncomms9779; pmid: 26508471
52. E. Ruska, The development of the electron microscope and of electron microscopy. *Rev. Mod. Phys.* **59**, 627–638 (1987). doi: 10.1103/RevModPhys.59.627
53. O. Scherzer, Über einige Fehler von Elektronenlinsen. *Z. Phys.* **101**, 593–603 (1936). doi: 10.1007/BF01349606
54. O. Scherzer, Spharische und Chromatische Korrektur von Elektronen-Linsen. *Optik* **2**, 114–132 (1947).
55. H. H. Rose, Historical aspects of aberration correction. *J. Electron Microsc.* **58**, 77–85 (2009). doi: 10.1093/jmicro/dfp012; pmid: 19254915
56. D. J. Smith, Development of aberration-corrected electron microscopy. *Microsc. Microanal.* **14**, 2–15 (2008). doi: 10.1017/S1431927608080124; pmid: 18171498
57. M. Haider *et al.*, Electron microscopy image enhanced. *Nature* **392**, 768–769 (1998). doi: 10.1038/33823
58. P. E. Batson, N. Dellby, O. L. Krivanek, Sub-ångstrom resolution using aberration corrected electron optics. *Nature* **418**, 617–620 (2002). doi: 10.1038/nature00972; pmid: 12167855
59. R. Erni, M. D. Rossell, C. Kisielowski, U. Dahmen, Atomic-resolution imaging with a sub-50-pm electron probe. *Phys. Rev. Lett.* **102**, 096101 (2009). doi: 10.1103/PhysRevLett.102.096101; pmid: 19392535
60. R. Hovden *et al.*, Breaking the Crowther limit: Combining depth-sectioning and tilt tomography for high-resolution, wide-field 3D reconstructions. *Ultramicroscopy* **140**, 26–31 (2014). doi: 10.1016/j.ultramic.2014.01.013; pmid: 24636875
61. J. G. Lozano *et al.*, Direct observation of depth-dependent atomic displacements associated with dislocations in gallium nitride. *Phys. Rev. Lett.* **113**, 135503 (2014). doi: 10.1103/PhysRevLett.113.135503; pmid: 25302902
62. G. Möbus, B. J. Inkson, Nanoscale tomography in materials science. *Mater. Today* **10**, 18–25 (2007). doi: 10.1016/S1369-7021(07)70304-8
63. M. Bar Sadan *et al.*, Toward atomic-scale bright-field electron tomography for the study of fullerene-like nanostructures. *Nano Lett.* **8**, 891–896 (2008). doi: 10.1021/nl073149i; pmid: 18237147
64. M. Koguchi *et al.*, Three-dimensional STEM for observing nanostructures. *J. Electron Microsc.* **50**, 235–241 (2001). doi: 10.1093/jmicro/50.3.235; pmid: 11469412
65. P. A. Midgley, M. Weyland, J. M. Thomas, B. F. G. Johnson, Z-contrast tomography: A technique in three-dimensional nanostructural analysis based on Rutherfordscattering. *Chem. Commun.* **2001**, 907–908 (2001). doi: 10.1039/b101819c
66. P. A. Midgley, M. Weyland, 3D electron microscopy in the physical sciences: The development of Z-contrast and EFTEM tomography. *Ultramicroscopy* **96**, 413–431 (2003). doi: 10.1016/S0304-3991(03)00105-0; pmid: 12871805
67. P. A. Midgley, R. E. Dunin-Borkowski, Electron tomography and holography in materials science. *Nat. Mater.* **8**, 271–280 (2009). doi: 10.1038/nmat2406; pmid: 19308086
68. I. Arslan, T. J. V. Yates, N. D. Browning, P. A. Midgley, Embedded nanostructures revealed in three dimensions. *Science* **309**, 2195–2198 (2005). doi: 10.1126/science.1116745; pmid: 16195455
69. H. L. Xin, P. Ercius, K. J. Hughes, J. R. Engstrom, D. A. Muller, Three-dimensional imaging of pore structures inside low-κ dielectrics. *Appl. Phys. Lett.* **96**, 223108 (2010). doi: 10.1063/1.3442496
70. S. Van Aert, K. J. Batenburg, M. D. Rossell, R. Erni, G. Van Tendeloo, Three-dimensional atomic imaging of crystalline nanoparticles. *Nature* **470**, 374–377 (2011). doi: 10.1038/nature09741; pmid: 21289625
71. S. J. Pennycook, P. D. Nellist, *Scanning Transmission Electron Microscopy: Imaging and Analysis* (Springer, 2011).
72. J. M. LeBeau, S. D. Findlay, L. J. Allen, S. Stemmer, Quantitative atomic resolution scanning transmission electron microscopy. *Phys. Rev. Lett.* **100**, 206101 (2008). doi: 10.1103/PhysRevLett.100.206101; pmid: 18518557
73. D. A. Muller, Structure and bonding at the atomic scale by scanning transmission electron microscopy. *Nat. Mater.* **8**, 263–270 (2009). doi: 10.1038/nmat2380; pmid: 19308085
74. R. F. Egerton, R. McLeod, F. Wang, M. Malac, Basic questions related to electron-induced sputtering in the TEM. *Ultramicroscopy* **110**, 991–997 (2010). doi: 10.1016/j.ultramic.2009.11.003
75. C. Ophus *et al.*, Efficient linear phase contrast in scanning transmission electron microscopy with matched illumination and detector interferometry. *Nat. Commun.* **7**, 10719 (2016). doi: 10.1038/ncomms10719; pmid: 26923483
76. K. Dabov, A. Foi, V. Katkovnik, K. Egiazarian, Image denoising by sparse 3-D transform-domain collaborative filtering. *IEEE Trans. Image Process.* **16**, 2080–2095 (2007). doi: 10.1109/TIP.2007.901238; pmid: 17688213
77. R. Gordon, R. Bender, G. T. Herman, Algebraic reconstruction techniques (ART) for three-dimensional electron microscopy and x-ray photography. *J. Theor. Biol.* **29**, 471–481 (1970). doi: 10.1016/0022-5193(70)90109-8; pmid: 5492997
78. A. H. Andersen, A. C. Kak, Simultaneous algebraic reconstruction technique (SART): A superior implementation of the art algorithm. *Ultrason. Imaging* **6**, 81–94 (1984). doi: 10.1177/016173468400600107; pmid: 6548059
79. P. Gilbert, Iterative methods for the three-dimensional reconstruction of an object from projections. *J. Theor. Biol.* **36**, 105–117 (1972). doi: 10.1016/0022-5193(72)90180-4; pmid: 5070894
80. J. Miao, F. Förster, O. Levi, Equally sloped tomography with oversampling reconstruction. *Phys. Rev. B* **72**, 052103 (2005). doi: 10.1103/PhysRevB.72.052103
81. E. Lee *et al.*, Radiation dose reduction and image enhancement in biological imaging through equally-sloped tomography. *J. Struct. Biol.* **164**, 221–227 (2008). doi: 10.1016/j.jsb.2008.07.011; pmid: 18771735
82. Y. Mao, B. P. Fahimian, S. J. Osher, J. Miao, Development and optimization of regularized tomographic reconstruction algorithms utilizing equally-sloped tomography. *IEEE Trans. Image Process.* **19**, 1259–1268 (2010). doi: 10.1109/TIP.2009.2039660; pmid: 20051344
83. Y. Zhao *et al.*, High-resolution, low-dose phase contrast x-ray tomography for 3D diagnosis of human breast cancers. *Proc. Natl. Acad. Sci. U.S.A.* **109**, 18290–18294 (2012). doi: 10.1073/pnas.1204460109; pmid: 23091003
84. B. P. Fahimian *et al.*, Radiation dose reduction in medical x-ray CT via Fourier-based iterative reconstruction. *Med. Phys.* **40**, 031914 (2013). doi: 10.1118/1.4791644; pmid: 23464329
85. A. Averbuch, R. Coifman, D. Donoho, M. Israeli, Y. Shkolnisky, A Framework for discrete integral transformations I—The pseudopolar Fourier transform. *SIAM J. Sci. Comput.* **30**, 764–784 (2008). doi: 10.1137/060650283
86. D. H. Bailey, P. N. Swarztrauber, The fractional Fourier transform and applications. *SIAM Rev.* **33**, 389–404 (1991). doi: 10.1137/1033097
87. Z. Saghi *et al.*, Three-dimensional morphology of iron oxide nanoparticles with reactive concave surfaces. A compressed sensing-electron tomography (CS-ET) approach. *Nano Lett.* **11**, 4666–4673 (2011). doi: 10.1021/nl202253a; pmid: 21950497
88. B. Goris, W. Van den Broek, K. J. Batenburg, H. Heidari Mezerji, S. Bals, Electron tomography based on a total variation minimization reconstruction technique. *Ultramicroscopy* **113**, 120–130 (2012). doi: 10.1016/j.ultramic.2011.11.004
89. R. Leary, Z. Saghi, P. A. Midgley, D. J. Holland, Compressed sensing electron tomography. *Ultramicroscopy* **131**, 70–91 (2013). doi: 10.1016/j.ultramic.2013.03.019; pmid: 23834932
90. O. Nicoletti *et al.*, Three-dimensional imaging of localized surface plasmon resonances of metal nanoparticles. *Nature* **502**, 80–84 (2013). doi: 10.1038/nature12469; pmid: 24091976
91. E. J. Kirkland, *Advanced Computing in Electron Microscopy* (Springer, ed. 2, 2010).

92. A. F. Brilot *et al*., Beam-induced motion of vitrified specimen on holey carbon film. *J. Struct. Biol.* **177**, 630–637 (2012). doi: 10.1016/j.jsb.2012.02.003; pmid: 22366277
93. D. Van Dyck, J. R. Jinschek, F.-R. Chen, 'Big Bang' tomography as a new route to atomic-resolution electron tomography. *Nature* **486**, 243–246 (2012). doi: 10.1038/nature11074; pmid: 22699616
94. K. S. Raines *et al*., Three-dimensional structure determination from a single view. *Nature* **463**, 214–217 (2010). doi: 10.1038/nature08705; pmid: 20016484
95. C. L. Jia *et al*., Determination of the 3D shape of a nanoscale crystal with atomic resolution from a single image. *Nat. Mater.* **13**, 1044–1049 (2014). doi: 10.1038/nmat4087; pmid: 25242534
96. P. B. Hirsch, R. W. Horne, M. J. Whelan, LXVIII. Direct observations of the arrangement and motion of dislocations in aluminium. *Philos. Mag.* **1**, 677–684 (1956). doi: 10.1080/14786435608244003
97. W. Bollmann, Interference effects in the electron microscopy of thin crystal foils. *Phys. Rev.* **103**, 1588–1589 (1956). doi: 10.1103/PhysRev.103.1588
98. J. W. Menter, The direct study by electron microscopy of crystal lattices and their imperfections. *Proc. R. Soc. London Ser. A* **236**, 119–135 (1956). doi: 10.1098/rspa.1956.0117
99. A. Howie, M. J. Whelan, Diffraction contrast of electron microscope images of crystal lattice defects. III. Results and experimental confirmation of the dynamical theory of dislocation image contrast. *Proc. R. Soc. London Ser. A* **267**, 206–230 (1962). doi: 10.1098/rspa.1962.0093
100. P. Rez, M. M. J. Treacy, Three-dimensional imaging of dislocations. *Nature* **503**, E1 (2013). doi: 10.1038/nature12660; pmid: 24256805
101. J. Miao *et al*., Reply to 'Three-dimensional imaging of dislocations'. *Nature* **503**, E2 (2013).
102. L. D. Marks, Wiener-filter enhancement of noisy HREM images. *Ultramicroscopy* **62**, 43–52 (1996). doi: 10.1016/0304-3991(95)00085-2; pmid: 22666916
103. M. J. Hÿtch, A. M. Minor, Observing and measuring strain in nanostructures and devices with transmission electron microscopy. *MRS Bull.* **39**, 138–146 (2014). doi: 10.1557/mrs.2014.4
104. M. Hÿtch, F. Houdellier, F. Hüe, E. Snoeck, Nanoscale holographic interferometry for strain measurements in electronic devices. *Nature* **453**, 1086–1089 (2008). doi: 10.1038/nature07049; pmid: 18563161
105. J. H. Warner, N. P. Young, A. I. Kirkland, G. A. D. Briggs, Resolving strain in carbon nanotubes at the atomic level. *Nat. Mater.* **10**, 958–962 (2011). doi: 10.1038/nmat3125; pmid: 21963574
106. B. C. Larson, W. Yang, G. E. Ice, J. D. Budai, J. Z. Tischler, Three-dimensional x-ray structural microscopy with submicrometre resolution. *Nature* **415**, 887–890 (2002). doi: 10.1038/415887a; pmid: 11859363
107. S. Kim *et al*., 3D strain measurement in electronic devices using through-focal annular dark-field imaging. *Ultramicroscopy* **146**, 1–5 (2014). doi: 10.1016/j.ultramic.2014.04.010; pmid: 24859824
108. R. Vincent, P. A. Midgley, Double conical beam-rocking system for measurement of integrated electron diffraction intensities. *Ultramicroscopy* **53**, 271–282 (1994). doi: 10.1016/0304-3991(94)90039-6
109. L. A. Beavan, R. M. Scanlan, D. N. Seidman, The defect structure of depleted zones in irradiated tungsten. *Acta Metall.* **19**, 1339–1350 (1971). doi: 10.1016/0001-6160(71)90071-X
110. B. Gault, M. P. Moody, J. M. Cairney, S. P. Ringer, in *Atom Probe Microscopy* (Springer Series in Materials Science, Springer, 2012), pp. 9–28.
111. M.-C. Daniel, D. Astruc, Gold nanoparticles: Assembly, supramolecular chemistry, quantum-size-related properties, and applications toward biology, catalysis, and nanotechnology. *Chem. Rev.* **104**, 293–346 (2004). doi: 10.1021/cr030698+; pmid: 14719978
112. P. D. Jadzinsky, G. Calero, C. J. Ackerson, D. A. Bushnell, R. D. Kornberg, Structure of a thiol monolayer-protected gold nanoparticle at 1.1 Å resolution. *Science* **318**, 430–433 (2007). doi: 10.1126/science.1148624; pmid: 17947577
113. W. W. Xu, Y. Gao, X. C. Zeng, Unraveling structures of protection ligands on gold nanoparticle $Au_{68}(SH)_{32}$. *Sci. Adv.* **1**, e1400211 (2015). doi: 10.1126/sciadv.1400211; pmid: 26601162
114. J. M. Yuk *et al*., High-resolution EM of colloidal nanocrystal growth using graphene liquid cells. *Science* **336**, 61–64 (2012). doi: 10.1126/science.1217654; pmid: 22491849
115. H. Elmlund, D. Elmlund, S. Bengio, PRIME: Probabilistic initial 3D model generation for single-particle cryo-electron microscopy. *Structure* **21**, 1299–1306 (2013). doi: 10.1016/j.str.2013.07.002; pmid: 23931142
116. R. G. Parr, W. Yang, *Density-Functional Theory of Atoms and Molecules* (Oxford Univ. Press, 1994).
117. Q. M. Ramasse *et al*., Probing the bonding and electronic structure of single atom dopants in graphene with electron energy loss spectroscopy. *Nano Lett.* **13**, 4989–4995 (2013). doi: 10.1021/nl304187e; pmid: 23259533
118. H. Lüth, *Solid Surfaces, Interfaces and Thin Films* (Springer, ed. 6, 2015).
119. W. H. Zachariasen, The atomic arrangement in glass. *J. Am. Chem. Soc.* **54**, 3841–3851 (1932). doi: 10.1021/ja01349a006
120. P. Bak, Icosahedral crystals: Where are the atoms? *Phys. Rev. Lett.* **56**, 861–864 (1986). doi: 10.1103/PhysRevLett.56.861; pmid: 10033305
121. H. Takakura, C. P. Gómez, A. Yamamoto, M. De Boissieu, A. P. Tsai, Atomic structure of the binary icosahedral Yb-Cd quasicrystal. *Nat. Mater.* **6**, 58–63 (2007). doi: 10.1038/nmat1799; pmid: 17160006
122. Y. Zhu, H. Dürr, The future of electron microscopy. *Phys. Today* **68**, 32–38 (2015). doi: 10.1063/PT.3.2747
123. K. W. Chapman, P. J. Chupas, C. J. Kepert, Selective recovery of dynamic guest structure in a nanoporous prussian blue through in situ x-ray diffraction: A differential pair distribution function analysis. *J. Am. Chem. Soc.* **127**, 11232–11233 (2005). doi: 10.1021/ja053266k; pmid: 16089438
124. E. L. Redmond, B. P. Setzler, P. Juhas, S. J. L. Billinge, T. F. Fuller, In-situ monitoring of particle growth at PEMFC cathode under accelerated cycling conditions. *Electrochem. Solid-State Lett.* **15**, B72–B74 (2012). doi: 10.1149/2.004206esl
125. H. Liu *et al*., Capturing metastable structures during high-rate cycling of $LiFePO_4$ nanoparticle electrodes. *Science* **344**, 1252817 (2014). doi: 10.1126/science.1252817; pmid: 24970091
126. Z. Huang *et al*., Grain rotation and lattice deformation during photoinduced chemical reactions revealed by in situ x-ray nanodiffraction. *Nat. Mater.* **14**, 691–695 (2015). doi: 10.1038/nmat4311; pmid: 26053760
127. T. Egami, S. J. L. Billinge, *Underneath the Bragg Peaks: Structural Analysis of Complex Materials* (Elsevier, ed. 2, 2012).
128. S. J. L. Billinge, I. Levin, The problem with determining atomic structure at the nanoscale. *Science* **316**, 561–565 (2007). doi: 10.1126/science.1135080; pmid: 17463280
129. D. A. Keen, A. L. Goodwin, The crystallography of correlated disorder. *Nature* **521**, 303–309 (2015). doi: 10.1038/nature14453; pmid: 25993960
130. V. Krayzman *et al*., A combined fit of total scattering and extended x-ray absorption fine structure data for local-structure determination in crystalline materials. *J. Appl. Cryst.* **42**, 867–877 (2009). doi: 10.1107/S0021889809023541
131. C. L. Farrow, C. Shi, P. Juhás, X. Peng, S. J. L. Billinge, Robust structure and morphology parameters for CdS nanoparticles by combining small-angle x-ray scattering and atomic pair distribution function data in a complex modeling framework. *J. Appl. Cryst.* **47**, 561–565 (2014). doi: 10.1107/S1600576713034055

ACKNOWLEDGMENTS

We thank U. Dahmen and M. C. Scott for stimulating discussions and Y. Yang, G. Melinte, C.-C. Chen, and I.-S. Chou for help with the figures and references. This work was primarily supported by the Office of Basic Energy Sciences of the U.S. Department of Energy (DOE) (grant DE-SC0010378). J.M. acknowledges the partial support by NSF (grant DMR-1437263), Office of Naval Research Multidisciplinary University Research Initiative (grant N00014-14-1-0675), and the Defense Advanced Research Projects Agency Program in Ultrafast Laser Science and Engineering through a grant from the Aviation and Missile Research, Development, and Engineering Center. P.E. acknowledges support for the Molecular Foundry, Lawrence Berkeley National Laboratory, which is supported by the DOE under contract no. DE-AC02-05CH11231. S.J.L.B. acknowledges support from NSF through grant DMR-1534910.

10.1126/science.aaf2157